

A molecular Rayleigh scattering setup to measure density fluctuations in thermal boundary layers

J. Panda¹ 

Received: 24 June 2016 / Revised: 13 September 2016 / Accepted: 20 October 2016 / Published online: 19 November 2016
© Springer-Verlag Berlin Heidelberg (outside the USA) 2016

Abstract A Rayleigh scattering-based density fluctuation measurement system was set up inside a low-speed wind tunnel of NASA Ames Research Center. The immediate goal was to study the thermal boundary layer on a heated flat plate. A large number of obstacles had to be overcome to set up the system, such as the removal of dust particles using air filters, the use of photoelectron counting electronics to measure low intensity light, an optical layout to minimize stray light contamination, the reduction in tunnel vibration, and an expanded calibration process to relate photoelectron arrival rate to air density close to the plate surface. To measure spectra of turbulent density fluctuations, a two-PMT cross-correlation system was used to minimize the shot noise floor. To validate the Rayleigh measurements, temperature fluctuations spectra were calculated from density spectra and then compared with temperature spectra measured with a cold-wire probe operated in constant current mode. The spectra from the downstream half of the plate were found to be in good agreement with cold-wire probe, whereas spectra from the leading edge differed. Various lessons learnt are discussed. It is believed that the present effort is the first measurement of density fluctuations spectra in a boundary layer flow.

1 Introduction

Measurement of various turbulence statistics in high-speed, compressible flows and heated flows is extremely difficult using current experimental techniques. In such flows

fluctuations in scalars such as density and temperature are as important as that of velocity; however, existing tools, such as particle image velocimetry, and intrusive probes, cannot measure density fluctuations. As for the measurement of temperature fluctuations, commercially available fine thermocouple probes are capable of a frequency range of a couple of 100 Hz, and a cold-wire constant current probe extends that to a couple of kHz, albeit for a small temperature range. The current endeavor is a part of an effort to develop a particle-free, non-intrusive, molecular Rayleigh scattering-based technique to simultaneously measure density, velocity, and temperature fluctuations in wind tunnel applications. Multiple obstacles exist for successful measurement. The present work, using a demonstration unit in a low-speed research tunnel, attempts to find the means to overcome these obstacles and provide a stepping stone for larger applications.

The molecular Rayleigh scattering technique provides a fundamental way of measuring flow properties of gases. For the present work, the measurement of air density is of interest. In the author's experience, in a new setup, once all steps for density measurement are implemented, optical spectral analysis to measure velocity and temperature becomes easier. The intensity of the Rayleigh scattered light is directly proportional to the molecular number density, which in turn is related to bulk density. The proportionality constant between the bulk density and the Rayleigh intensity is obtained via a calibration procedure. Once the time variation of the scattered light intensity was measured, a Fourier transform and an application of the calibration constants provided spectra of air density fluctuations. The technique has been used extensively in high-speed free jets (Panda and Seasholtz 1999, 2002; Mielke et al. 2009 among others), and premixed combusting flows (Pitts and Kashiwagi 1984; Ng et al. 1982; Robben

✉ J. Panda
Jayanta.Panda-1@nasa.gov

¹ NASA Ames Research Center, Moffett Field, CA, USA

1975) and provided unprecedented insight into unsteadiness of shock structure, fluctuations responsible for sound radiation, behavior of combustion process, and modeling constants for CFD simulations. All of these applications involved open jets where the confinements of a wind tunnel were absent. Poggie et al. (2004) used Rayleigh scattering from condensation of H₂O and CO₂ molecules in supersonic wind tunnels to visualize boundary layer structures. There have been a few efforts (for example, Balla 2015) to use Rayleigh scattering techniques in high-speed wind tunnels; however, mostly time-averaged quantities such as time-averaged gas density could be measured. Quantitative unsteady measurements in wind tunnel environments require overcoming challenges associated with the insertion of the laser beam, containment of specular and diffused reflection, removal of dust particles, and adequate vibration isolation. The first objective of the present work is to demonstrate the applicability of Rayleigh scattering for wind tunnel test by overcoming each of the above difficulties. The second objective is to study turbulent density fluctuations in thermal boundary layers created over a flat plate with zero pressure gradient.

Boundary layers on heated flat plates have been studied by multiple researchers in the past. Some of the classical work leading to the semi-empirical relations for heat transfer is summarized by Schlichting (1979). Ohta and Hirokazu (2014) analyzed a DNS database of a low Reynolds number turbulent boundary layer in terms of density fluctuations and identified various vorticity dynamics. They associated acoustic emission to density fluctuations. Sohn and Reshotko (1991) surveyed mildly heated thermal boundary layers on a flat plate using hot-film probes. They also measured velocity–temperature correlation parameters. Simonich and Bradshaw (1978) performed measurements on a boundary layer in zero pressure gradient and showed that grid-generated free-stream turbulence increased heat transfer by approximately five percent for each one percent increase in the longitudinal velocity fluctuations. All of these measurements used traditional hot-wire probes that are intrusive and have limited applicable temperature and velocity ranges.

1.1 Laser Rayleigh scattering

When a laser beam is allowed to pass through a gas, the molecules present cause inelastic and elastic light scattering. The inelastic scattering is called Raman scattering, and the elastic scattering is called Rayleigh scattering. The Raman scattering cross section is far weaker than that of Rayleigh. Moreover, for gas density measurement, the variation of the total light intensity with the molecular number density is of interest. Since this variation is identical for both Rayleigh and Raman scattering processes,

a separation between the two is unnecessary. The following considers the Rayleigh scattered part where the power of the scattered light, P_s , collected from a probe volume, V_{sc} into a solid angle, $d\Omega$, can be written as the following (Robben 1975):

$$P_s = m I_0 V_{sc} \left(\sum_j \mu_j \frac{\partial \sigma_j}{\partial \Omega} \right) \sin^2 \chi \, d\Omega = k' m \quad (1)$$

here m is the molecular number density, I_0 is the incident light irradiance (W/m²), $\partial \sigma_j / \partial \Omega$ is the Rayleigh scattering cross section of the species j in the gas mixture, μ_j is the mole fraction of species j , and χ is the angle between the incident electric vector and the direction of light collection. The Rayleigh scattering cross section depends on the refractive index of the particular species and is constant for a fixed wavelength laser and a fixed gas mixture (air for this work). For a fixed optical setup, the scattered laser power is directly proportional to the molecular number density. Now, the number density m is related to the bulk density, ρ through the following:

$$m = \frac{\rho N_A}{M}, \quad (2)$$

where M is the molar mass and N_A is the Avogadro constant (6.022×10^{26} kmol⁻¹). The scattered light intensity was measured using a photomultiplier tube, and a photon-counting process was performed. The number of photons collected during a fixed time interval Δt can be written as:

$$N = \frac{\varepsilon P_s \Delta t}{h\nu} = \frac{\varepsilon \rho N_A I_0 V_{sc} \left(\sum_j \mu_j \frac{\partial \sigma_j}{\partial \Omega} \right) \sin^2 \chi \, d\Omega \, \Delta t}{M h \nu} = k \rho \, \Delta t \quad (3)$$

where, h is the Planck constant (6.626×10^{-34} J s), ν is the frequency of the laser light, and ε is the overall collection efficiency (a product of the light transmission efficiency and the quantum efficiency of the photomultiplier tube). Equation 3 shows that the photon count over a fixed time interval is directly proportional to the gas density within the probe volume. The proportionality constant k has to be determined through a calibration process. For the wind tunnel setup, the expected photoelectron rate at ambient condition can be estimated as the following. Note that the probe volume V_{sc} is the volume of the laser beam imaged on the collection fiber; it is determined by the magnification ratio (1.5 for the present setup) times the diameter of the collection fiber (0.6 mm) times the laser beam cross-sectional area.

$$V_{sc} = 0.0009 \times (\text{laser beam cross section})\text{m}^3.$$

A 400-mW laser was used for the present setup; therefore, the incident irradiance I_0 is the following:

$$I_0 = 0.4/(\text{laser beam cross section}) J/(\text{m}^2 \text{ s});$$

$$\text{Differential cross section of air for } 532 \text{ nm light} = 5.24 \times 10^{-31}/4\pi \text{ m}^2/\text{Sr};$$

$$d\Omega = 0.49 \text{ Sr (} f/4 \text{ collection lens);}$$

$$\chi = 90^\circ \text{ (efficient orientation of beam polarization);}$$

$$\rho = 1.1 \text{ kg/m}^3;$$

$$M = 28.97 \text{ kg/kmol};$$

$$\varepsilon = 0.06; \text{ (assumed)}$$

$$N \sim 2.7 \times 10^6/\text{s}.$$

The advantage of the photon-counting approach over the conventional measurement of analog PMT output (Pitts and Kashiwagi 1984) is a clearer estimate of measurement uncertainty due to electronic shot noise. A commercially available, PC-based, multi-scalar counter was used for this purpose. The multi-scalar allowed for photoelectron counting over 2,621,440 contiguous time bins of user-specified time duration.

2 Experimental setup

After evaluating a series of small wind tunnels at NASA Ames, it was finally decided to create the Rayleigh setup in a low-speed, in-draft tunnel (“blue” tunnel) that provided the necessary ease of access and ease of modifications. Air flow in the velocity range of 0–46 m/s through the 0.38 m × 0.38 m × 1.22 m test section was created by a variable speed blower which drew ambient air through a 1.22 m × 1.22 m inlet section, a series of turbulence management screens, and a 10.24:1 area contraction section (Fig. 1). The test article was a pair of 0.305 m (length) × 0.23 m (width) flat plates and a 1 kW electrical strip heater sandwiched between the two. Layers of fiber glass insulation were placed between the heater and the bottom plate to reduce heat loss through the bottom

surface. The strip heater was connected to a variable voltage AC power supply that heated the top plate to a wide range of temperatures. The plate was traversed vertically for a boundary layer survey, using an automated traversing stage. The top surface was painted flat black with high temperature spray paint to minimize stray scattering especially when the laser beam was brought very close to the plate surface.

2.1 Optical arrangement

For the light source a small profile, solid-state, diode-pumped, continuous-wave, laser source was selected that produced linearly polarized light with 100:1 polarization ratio, and 400 mW of power at 532 nm wavelength. The laser was oriented such that the polarization axis remained perpendicular to the collection direction, which maximized the scattering intensity toward the collection direction.

An important factor for a successful Rayleigh setup is an effective containment of the stray scattered light. This is somewhat easier in a jet facility since the laser source and the beam dump can be kept outside of the jet flow. That is one of the main reason for most of the past Rayleigh setups to be created around free jets. In a wind tunnel if the laser beam was directly inserted through a glass wall or a window then the scattering from these surfaces would be a large fraction of the Rayleigh scattered light. Rayleigh scattering is an elastic process; the scattered light is in the same frequency as that of the incident beam, except for the Doppler shift caused by the moving gas. In low-speed flows, the Doppler shift is fairly small, which makes separation of the Rayleigh scattered light from the stray scattering difficult. Therefore, the preferred path is to minimize the stray scattering as much as possible. For the present effort, two different forms of insertion were attempted. For the first setup, a small profile laser source was mounted directly inside the

Fig. 1 Rayleigh scattering setup in the low-speed wind tunnel, a periscopic probe was used to deliver the laser beam

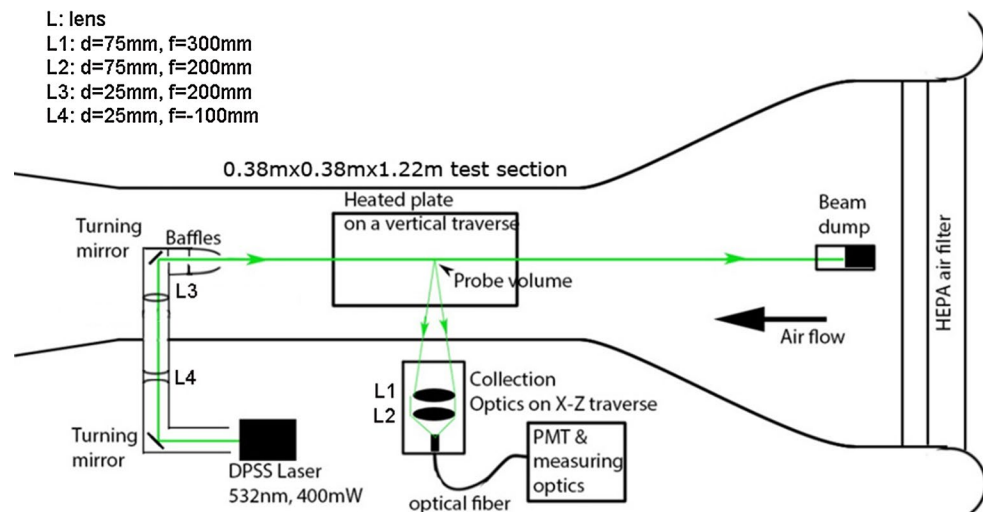
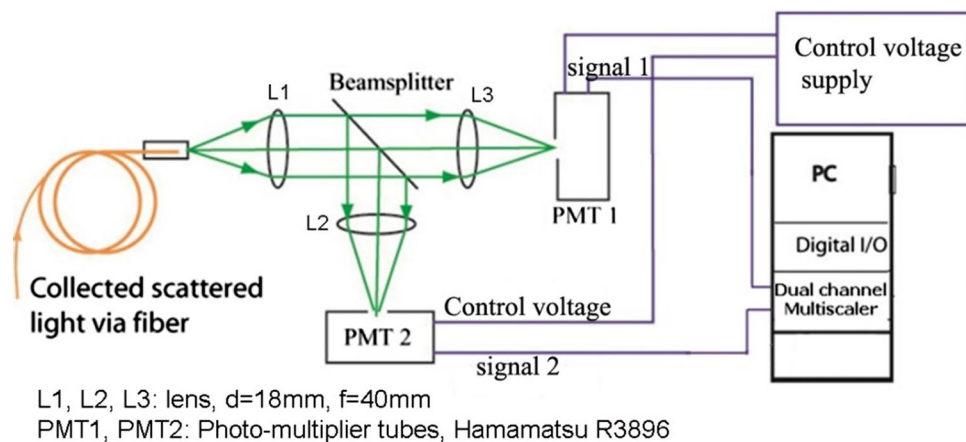


Fig. 2 Dual PMT setup to measure fluctuations in Rayleigh scattered light



tunnel (Panda and Schery 2014), while for the second setup the laser source was mounted outside the test section and the beam was passed through a delivery probe made of two turning mirrors, two lens, and multiple baffles; all mounted in a 30-mm-diameter hollow tube (Fig. 1). The tube passed through the tunnel wall. The lens inside the tube blocked air leakage, and the baffles minimized stray light around the laser beam. In either of the setups, complete elimination of forward propagating stray light was impossible, but was significantly reduced. The laser beam passed from downstream of the test article to the upstream direction and was ultimately terminated upstream in a small profile beam-dump placed ahead of the wind tunnel contraction section. At its waist, the laser beam profile was measured to be Gaussian with a full-width at half-maxima of 0.3 mm; the beam diverged slightly from the waist.

The beam dump design and placement were found to be important in the management of the stray light. To reduce wake turbulence, the beam dump was placed 1.8 m upstream of the plate and upstream of the contraction section. To reduce the aerodynamic blockage, one would like to place as small a beam dump as possible; yet, the dump needs to be large enough to contain the diverging, larger diameter beam turning by the thermal boundary layer. At first a smaller 20 mm \times 20 mm profile beam dump was used. However, it was observed that the laser beam while passing parallel to the heated plate experienced a steering effect from the thermal boundary layer. The beam motion was directly related to the plate temperature and the proximity to the plate surface. The steering caused the beam to move in and out of the dump which significantly increased the background flicker. Therefore, a larger 38 mm \times 32 mm profile beam dump had to be used to contain the wandering beam. The alignment was made such that in the unheated condition, the laser beam impinged on the lower part of the opening (the density gradient in the boundary layer deflected the beam upwards). In effect, the beam dump acted as a bluff body placed in the very low

speed air stream; the wake from this bluff body was attenuated while passing through the contraction section. Still the free-stream turbulence level at the test section was found to be increased by an additional 0.05%. Although the dump effectively absorbed the laser beam, still stray reflected light leaked out through the large opening and slightly illuminated the leading edge of the flat plate.

The molecular scattered light from a small region on the beam was collected and measured using photomultiplier tubes (PMT). The collection optics was made of a pair of 75-mm-diameter achromatic lenses that focused the scattered light on a multi-mode optical fiber (Fig. 1). The fiber core diameter of 0.6 mm, and the 1.5 magnification ratio of the collection lens system, fixed the length of the probe volume to 0.9 mm. The setup was for a point measurement along the beam path. The scattered light collected by the receiving fiber was transmitted to a separate set of optics (Fig. 2), where it was collimated and then split into two equal parts by a thin-film beam splitter. Each of the beams was refocused into individual photomultiplier tubes. Photon-counting electronics were then used to measure light intensities. To minimize the stray light collection, the back wall of the wind tunnel was painted flat black.

2.2 Aerosol filtration system

Any practical application of the Rayleigh scattering technique requires multiple strategies to minimize the effect of Mie scattering from aerosol particles naturally present in the air stream. A two prong approach was undertaken: a hardware approach of thorough cleaning of the air stream, and a software approach of identification and removal of the signature from the passage of dust particles.

2.3 Cleaning of the air stream

The concentration of the dust particles in the airstream was studied systematically. At first, the particle content in the

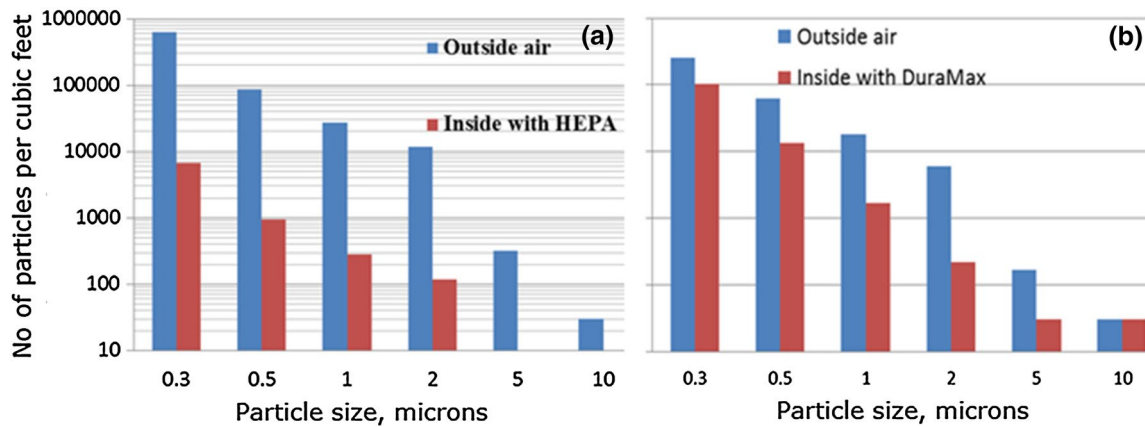


Fig. 3 Effectiveness of **a** HEPA® filter and **b** 95% efficient Duramax® filter in reducing dust particles in the wind tunnel facility. Data from two different days

ambient air and inside the wind tunnel, in the size range of 0.3–10 micron, was measured with an aerosol counter. It was found that the existing coarse filter hardly reduced the particle counts inside the stream. This pointed to the need of using better air filters. Additionally, the wind tunnel screens and the wall surfaces were thoroughly cleaned of the dust particles that accumulated over many years of operation (some from the use of particle-based techniques). In the next step, better air filters were placed at the inlet. Typically air filters that provide increased cleaning also create a larger pressure drop. The latter is specified as the allowable maximum velocity on the filter inlet. For example, a maximum allowable face velocity of 4.5 m/s leads to a maximum test section velocity of roughly 46 m/s. A path to overcome this limitation would be to build a larger air intake chamber around the wind tunnel inlet. However, the goal of the experiment was to reach a maximum of 30 m/s speed, and therefore, no additional chamber was built. Nonetheless, at first a lower 95% filtration efficiency Duramax air filter was used, and then, a 99.9% HEPA filter was used. Comparisons of particle counts and filtration efficiencies achieved with these two different filters are shown in Fig. 3. Note that in the absence of the filters there was little difference in the particle counts between the test section and the outside ambient air. Compared to the lower efficiency filter, the HEPA filter restricted the maximum allowable flow rate by an additional 15%; still it was chosen for significantly lowering the aerosol concentration in the test section. It is worth noting that the particle count in the ambient air in the urban area where NASA Ames center is located is dependent on the level of pollution and other factors. On a clear winter day, after a rainstorm, the particle counts could be lower by a factor of 20 compared to that in a highly polluted day. The use of the HEPA filter is expected to minimize impact of this variation.

2.4 Software approach of cleaning particle trace

The passage of particles was accompanied by a sharp rise in the count rate. As mentioned earlier, the present setup uses photoelectron counts in contiguous series of time bins. Figure 4 shows two such time series obtained using two different air filters. The drastic reduction in the particle count, when HEPA filter was used, allowed for longer bin time (Fig. 4b), which leads to higher count and improvement in signal-to-noise ratio. photoelectron count follows Poisson's statistics; therefore, even when there is no variation in light intensity the count rate fluctuates within a limit. The passage of particles created a far larger swing. A close-up view of a small region in one of the time traces is shown in Fig. 5. Data points where the count rate was larger than five times the standard deviation were replaced by the average count:

$$\text{If } N_i \geq KN_{\text{stddev}}, N_i = N_{\text{av}}, K = 5 \quad (4)$$

The blue lines in Figs. 4 and 5 were obtained by this means. Although mostly successful, a drawback of this process is that the relatively weaker signature from smaller particles, or particles passing through the outskirts of the Gaussian laser beam, could not be removed. This was found to increase the noise floor of the spectrum calculated from the time trace. Nevertheless, it was nearly impossible to remove all dust particles in a wind tunnel flow, and when the numbers of dust particles were few, the peak stripping technique was effective.

2.5 Vibration isolation

The blower in the wind tunnel created vibration that was found to be transmitted to the test section via the metal duct

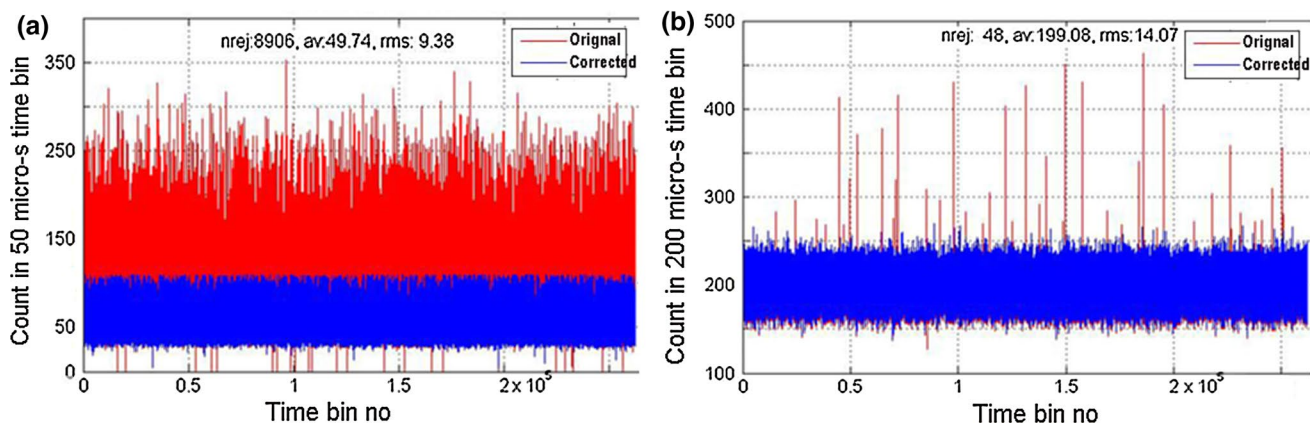


Fig. 4 Time traces of photoelectron count before and after software cleaning when **a** the lower efficiency filter was used **b** the higher efficiency HEPA filter was used. Note, different bin-time duration

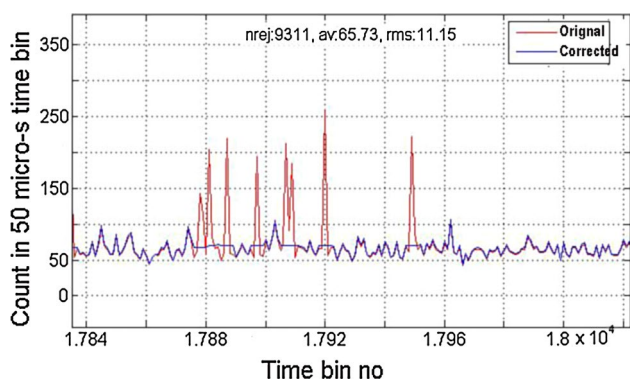


Fig. 5 Software removal of particle signature from time trace of photoelectron count (zoomed-in view of a small section of data shown in Fig. 4a)

to which the blower inlet was connected, as well as through the ground. An effective solution to isolate vibration transmitted through the ground was obtained by placing the optical components on a pneumatically isolated breadboard support frame. Isolation from vibration of the test section wall was somewhat more difficult; any small contact with the wind tunnel wall was found to vibrate the optical components. Therefore, holes slightly bigger than the supporting rods were cut on the tunnel floor. This caused a small leakage of air.

3 Results and discussion

The Rayleigh scattering setup measured the intensity of the scattered light using a two photomultiplier setup shown earlier in Fig. 2. A dual channel multi-scalar performed photoelectron counting in $n = 2,621,440$ contiguous bins duration (N_i , $i = 1, 2, \dots, n$). The time duration of each bin

was varied between 50 and 200 μs , which effectively created variations in sampling rate of 20,000–5000/s. Typical commercial multi-scalars provide options to change the bin duration over a wide range of time intervals: from several nanoseconds to several milliseconds. Therefore, there exists no practical limitation on the upper limit of the sampling rate.

3.1 Density calibration

After removing the particle signature, a pulse pile-up correction was made on each data point (Hamamatsu 2007):

$$\dot{N}_{i\text{-correct}} = \dot{N}_{i\text{-meas}} / (1 - \Delta t_{\text{pair}} \dot{N}_{i\text{-meas}}) \quad (5)$$

here, Δt_{pair} is the minimum time difference between two photoelectron pulses necessary for the counter to make distinction (20 ns for the present instrument). The time average of the counts represented the average intensity of the Rayleigh scattered light from the probe volume. A calibration process was necessary to determine the proportionality constant between the photon count rate and the air density. An outstanding issue with measurements close to the wall was large changes in the intensity of the scattered light even when the plate was unheated, i.e., in uniform air density (Fig. 6). There were multiple reasons for this non-uniformity. The primary one was a blockage of the field of view of the collection optics as the plate was brought close to the beam, i.e., the effective solid angle for light collection was reduced, which in turn lowered the measured photoelectron rate. However, proximity to the plate also meant increased background illumination. Both the stray forward scattered light around the laser beam and backscattered light from the beam dump were increased. This created a visible increase in the background illumination. Except for the locations very close to the plate, the decrease in intensity due to the blockage exceeded the increase due to a

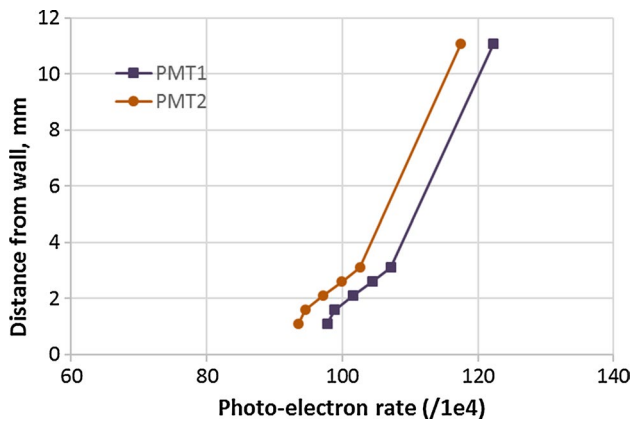


Fig. 6 Variation of photoelectron count rate with distance from the wall, unheated plate, $x/L = 0.79$

brighter background, resulting into a general lowering of the count rate. Since the combined effect cannot be modeled, the calibration procedure involving density versus photoelectron rate had to be performed at multiple heights above the plate surface.

A Dantec® cold-wire temperature probe, operated in constant current anemometer (CCA) mode, was brought to the same height as that of the center of the laser probe volume to measure the local temperature. The probe was lifted up, laser turned on, and photoelectron counting performed to measure scattering intensity. The procedure was repeated for several plate temperatures. Figure 7 shows the calibration curves for both PMTs. The local density ρ was determined from ideal gas law, and by knowing the ambient pressure. A straight line was fitted through each data set obtained at a given height above the wall. If N_{av} is the average count over a time interval Δt , and ρ is the local density,

then each calibration curve provides a pair of constants a and b .

$$N_{av} = (a\rho + b) \Delta t, \quad \text{where } N_{av} = \frac{\sum N_i}{n} \quad (6)$$

The calibration constants, obtained from least square fits, are shown in the legend of Fig. 7. Since the thicknesses of the thermal boundary layers were fairly small, a limited temperature (density) range was available for points further away from the plate. This limited range created higher uncertainty in the calibration constants for points away from the plate surface. The goodness of fit R^2 values, shown in the legend, provides measures of the associated uncertainty. The intercepts of the linear fits represent part of the count independent of density change, and for the most part, representative of the extent of contamination by stray scattering. For the present setup, the collection lens was exposed to the back wall of the wind tunnel and the light scattered from the wall contributed to the relatively larger value of the intercept. In spite of many precautions described above, some amount of stray light contamination is inevitable. It is believed that the rigorous calibration applied in the present study has mostly accounted for the stray background. Nevertheless, a change in the value of the constant b is expected to affect the value of a , which was used to convert the fluctuating part of light intensity to the physical fluctuations in density.

3.2 Time average density, density fluctuations spectra, and root-mean-square measurements

The instantaneous flow density ρ is divided into a time-averaged part $\bar{\rho}$ and a fluctuating part ρ'

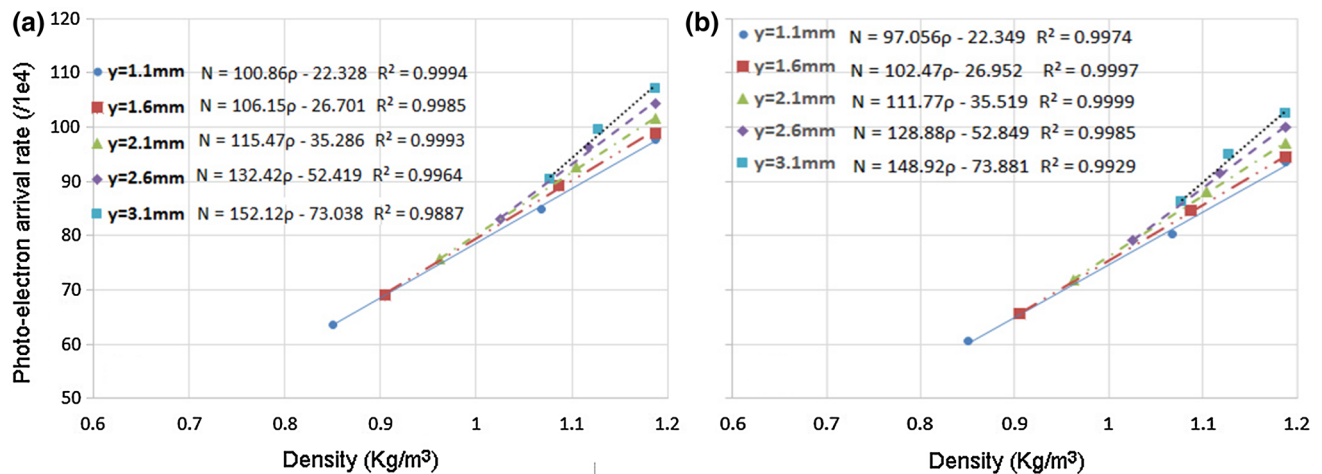


Fig. 7 Variations of the photoelectron count rates with air density measured at the indicated distances from the wall, and $x/L = 0.79$; **a** PMT1, **b** PMT2; equations in the legend show the calibration constants and the goodness of fit

$$\rho = \bar{\rho} + \rho' \tag{7}$$

The mean density was related to the average of all bins N_{av} :

$$\bar{\rho} = \frac{1}{a} \left(\frac{N_{av}}{\Delta t} - b \right) \tag{8}$$

However, the measurement of the fluctuating part was not straightforward, since the electronic shot noise arriving from the photomultiplier tube needed to be considered. Even when the incident light was of constant intensity (no density fluctuation), the rate of photoelectron emission by a PMT showed significant variation referred to as statistical photon count noise or “shot noise.” This noise was random in nature and followed Poisson’s statistics. The density fluctuations caused the collected light intensity to vary, and the problem became to separate the density fluctuations from the joint statistics of shot noise and physical light intensity variation. Toward this end a two-PMT cross-correlation procedure was employed (Panda and Seasholtz 2002).

As mentioned earlier, the collected light was split into two parts and measured with two PMTs. The simultaneous photoelectron counting produced two series of data N_{1i} and N_{2i} ($i = 0, 1, 2, \dots, n-1$). The average values from each of the time series were subtracted: $N_{1i}' = N_{1i} - N_{1av}$, $N_{2i}' = N_{2i} - N_{2av}$, and discrete, one-sided auto-spectra were calculated, which are subsequently multiplied by appropriate calibration constants.

$$|\varphi_{N_1'}(f_l)| = \frac{2}{n^2} |F_{N_1'}(l)|^2, \tag{9}$$

where, $F_{N'}(l) = \sum_{i=0}^{n-1} N_i' \exp \left(j \frac{2\pi i l}{n} \right)$,

$$f_l = \frac{l}{n\Delta t} \quad l = 0, 1, 2, \dots, \frac{n}{2} - 1$$

The upper two lines in Fig. 8 show the auto-spectra from an unheated plume where there are no actual density fluctuations. The relatively large energy level in the spectra was entirely due to the electronic shot noise in the photoelectron count. The two series of data were then used to determine one-sided, cross-spectral density:

$$|\varphi_{N_1' N_2'}(f_l)| = \frac{2}{n^2} |F_{N_1'}(l) \cdot F_{N_2'}^*(l)|, \tag{10}$$

Superscript * in the above equation indicates the complex conjugate. The density fluctuation spectrum was calculated using appropriate calibration constants a_1 and a_2 for the two photomultiplier tubes:

$$\varphi_{\rho^2}(f_l) = \frac{|\varphi_{N_1' N_2'}(f_l)|}{a_1 a_2 (\Delta t)^2} \tag{11}$$

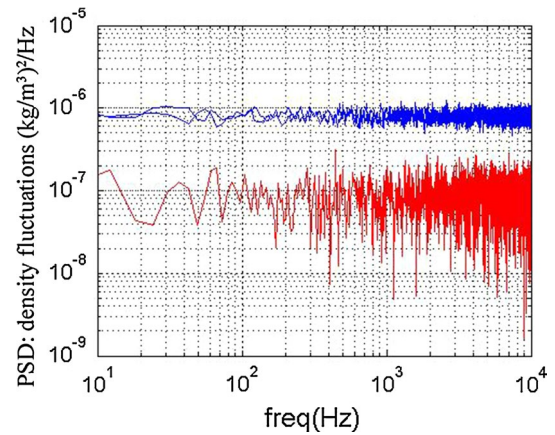


Fig. 8 Density fluctuations spectra measured from low-speed, unheated plume (without actual air density fluctuation). *Blue lines* power spectra from individual PMT; *red line* cross-spectral density between the two PMT

The bottom line in Fig. 8 shows the consequence of cross-spectral estimates; the shot noise contribution is reduced by a factor of 10 over the entire spectra. The remaining energy is partially due to insufficient convergence and partially due to the dust particles whose signatures were recorded by both PMTs. The root-mean-square of the density fluctuations can be calculated by integrating the cross-spectra

$$\rho'_{rms} = \sqrt{\sum_f \varphi_{\rho^2} \Delta f} \tag{12}$$

Figure 9a shows a set of power spectra at various heights above the plate for one fixed plate temperature. The axial station was close to the plate trailing edge. This figure demonstrates the wide dynamic range achievable with the setup. The signal-to-noise floor ratio was $>10^2$. The very low speed flow did not have much energy above approximately 2 kHz where the spectral data merged with the noise floor. It is expected that a similar setup would be able to resolve much wider frequency band in higher speed flows.

3.2.1 Validation of spectral data

To validate the density fluctuation spectra, a second method of measurement was required; however, this was unavailable. Therefore, an indirect path was pursued where temperature fluctuation spectra were estimated from the density data assuming pressure fluctuations to be insignificant inside the boundary layer, and fluctuations in the second order to be much smaller than the first-order quantities: $\rho' T' \ll \rho' T, T' \rho$. This provided the following relation for spectrum φ :

$$\varphi_{T^2}(f_l) = \left(\frac{\bar{T}}{\bar{\rho}} \right)^2 \varphi_{\rho^2}(f_l) \tag{13}$$

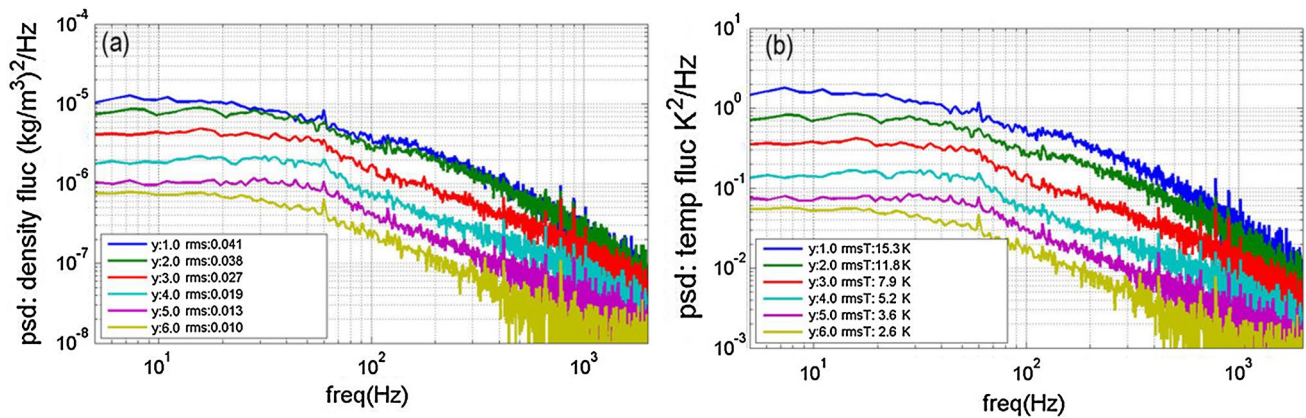


Fig. 9 **a** Rayleigh measurement of density fluctuations spectra from $x/L = 0.79$, plate centerline, and at indicated heights (mm) from the wall, $U_e = 9.8$ m/s, plate heated with 950 W; **b** spectra of temperature fluctuations derived from density; rms levels are shown in legend

Here the over bar denotes time average and the prime represents fluctuation around mean. Figure 9b shows the derived spectra. It is to be noted that the spectroscopic analysis of the Rayleigh scattered light is capable of directly providing temperature and its spectra (Mielke et al. 2009). That will be attempted at a later time. For the present purpose, the derived spectra of temperature fluctuations were compared with those measured with a Dantec miniature, cold-wire temperature probe and a Dantec constant current anemometer. The probe was placed at the same location of the Rayleigh probe volume, and the laser source was turned off. Time traces of anemometer voltage output were measured by a 24-bit digitization unit, and then, the vendor-provided calibration (temperature coefficient of the resistance change) was used to determine temperature history. The frequency response of the cold-wire probe was expected to be >1 kHz. In spite of the uncertainty in the probe location (the cold-wire diameter was 1 micron, while that of the laser beam about 0.3 mm), the two sets show good similarity which brings confidence in the Rayleigh data (Fig. 10). It is to be noted that such similarity was found from data collected at the downstream half of the plate, but that from the upstream half differed (not shown).

The primary difficulty with the current setup was found to be due to the beam steering caused by the thin thermal boundary layer when the beam was positioned in close proximity to the plate. The beam passed from the trailing edge to the leading edge of the plate. The thermal steering produced small but increasing wandering toward the leading edge. Since the intensity distribution in the beam was Gaussian, the wandering created fluctuations in the collected light intensity. The fluctuations due to the beam steering could not be separated from the desired part of the signal and were found to overwhelm the turbulence signature collected from the upstream half of the plate. Beam steering is inevitable when light waves

pass through an extended length of the thermal boundary layer. A possible remedy can be a redesign of the optical path, where the laser beam is positioned perpendicular to the plate.

4 Summary and conclusion

This paper describes an effort to setup a Rayleigh scattering-based measurement technique in a low-speed wind tunnel. The experiences gathered should prove valuable for future applications in larger and faster wind tunnels. The present effort started from the very basic step of identifying each optical component and progressed toward a working setup in a low-speed wind tunnel. For the molecular Rayleigh scattering setup, at first the air stream was cleansed of dust particles using HEPA filters. Then various steps were taken to reduce the vibration level created by the wind tunnel and transmission of vibration to various optical components. Another important factor was the minimization of stray light which required design of an optical train that minimized forward scattering from the insertion of the laser beam to the test section, and from the effective absorption in a beam dump. The beam was passed parallel to the heated plate and was brought within 0.7 mm from the surface. The field of view of the collection optics was found to be progressively obstructed as the beam was brought closer to the plate. Therefore, different calibration curves had to be constructed for different heights of the beam from the plate surface. The calibration curves related air density to the intensity of molecular scattered light. The latter was measured as the rate of photoelectron arrival using a two PMT system. Long records of photoelectron counting over contiguous time bins provided time histories of air density fluctuations which were Fourier transformed to obtain spectra of density fluctuations.

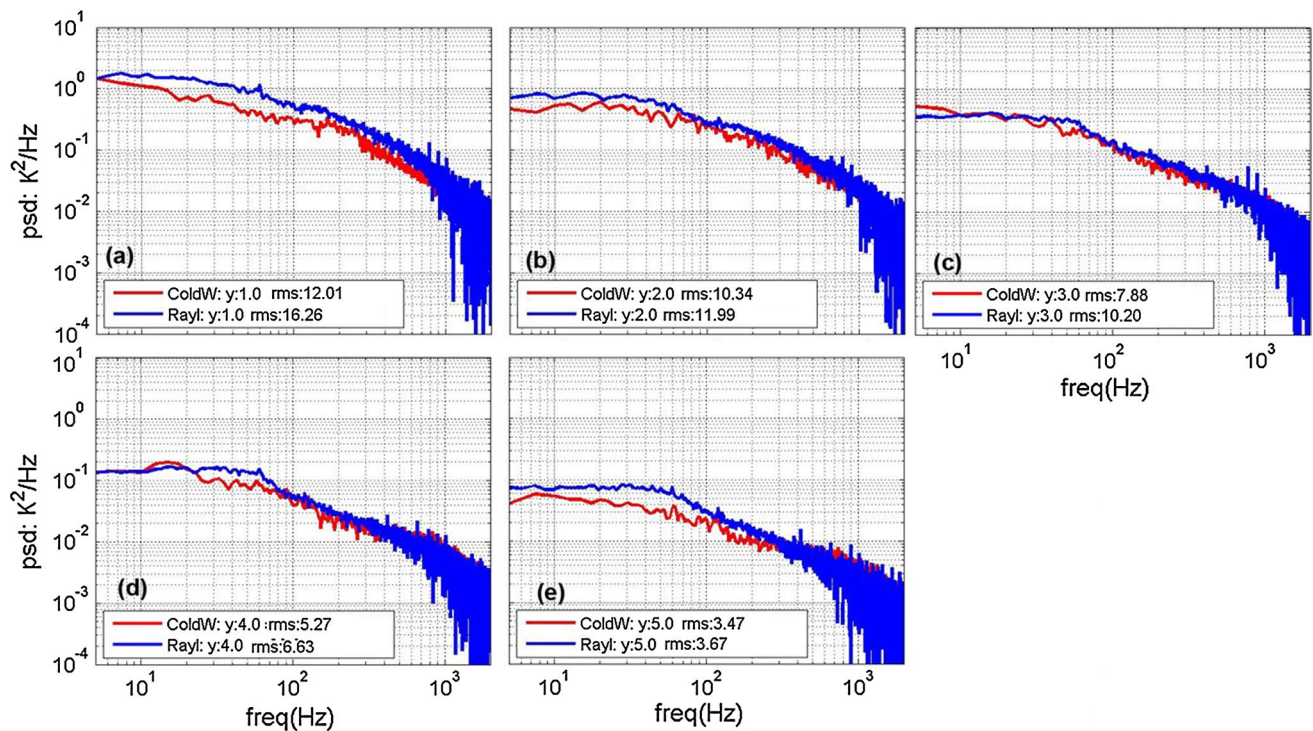


Fig. 10 Comparison of temperature fluctuations spectra measured using a cold-wire probe and via Rayleigh scattering at $x/L = 0.79$, $U_e = 9.8$ m/s, and 950 W of heating; probe height above the plate in mm, and rms level are shown in the legend

To validate measurements of density fluctuations, an indirect path was followed. At first spectra of temperature fluctuations were estimated from the density spectra assuming fluctuations of pressure to be negligible. Then spectra of temperature fluctuations were directly measured using a cold-wire operated in constant current mode. Excellent comparison from probe locations at the downstream part of the plate validated the Rayleigh technique. However, poor comparison from probe locations at the upstream half of the plate pointed out a problem associated with the steering of the beam by the strong thermal gradient close to the plate surface.

Acknowledgements The work was supported by NASA ARMD Innovative Measurement project with Dr. Tom Jones of NASA Langley as the manager.

References

- Balla RJ (2015) Mach 10 Rayleigh scattering gas-cap density, pressure and shock-jump measurements. *AIAA J* 53(3):756–762
- Hamamatsu Photonics K. K. (2007) Photomultiplier tubes, basics and applications, 3a edn. p 131
- Mielke AF, Elam KA, Sung C-J (2009) Multiproperty measurements at high sampling rates using Rayleigh scattering. *AIAA J* 47(4):850–862
- Ng TT, Cheng RK, Robben F, Talbot L (1982) Combustion–turbulence interaction in the turbulent boundary layer over a hot surface. Lawrence Berkeley Laboratory report LBL-13893
- Ohta T, Hirokazu K (2014) Structure of density fluctuations at a low-mach number turbulent boundary layer by DNS. *Flow Turbul Combust* 92:347–360
- Panda J, Schery SD (2014) Molecular Rayleigh scattering to measure fluctuations in density in low speed heated wind tunnel flows. *AIAA* 2014–2529. doi:10.2514/6.2014-2529
- Panda J, Seasholtz RG (1999) Shock structure and shock–vortex interaction in screeching jets measured using Rayleigh scattering. *Phys Fluids* 11(12):3761–3777
- Panda J, Seasholtz RG (2002) Experimental investigation of density fluctuations in high speed jets and correlation with generated noise. *J Fluid Mech* 450:97–130
- Pitts WM, Kashiwagi T (1984) The application of laser-induced Rayleigh scattering to the study of turbulence mixing. *J Fluid Mech* 141:391–429
- Poggie J, Erbland PJ, Smits AJ, Miles RB (2004) Quantitative visualization of compressible turbulent shear flows using condensate-enhanced Rayleigh scattering. *Exp Fluids* 37:438–454
- Robben F (1975) Comparison of density and temperature measurement using Raman scattering and Rayleigh scattering. Lawrence Berkeley report no: LBL-3294
- Schlichting H (1979) *Boundary layer theory*, 7th edn. McGraw-Hill, New York
- Simonich JC, Bradshaw P (1978) Effect of free-stream turbulence on heat transfer through a turbulent boundary layer. *J Heat Transf* 100(4):671–677
- Sohn K-H, Reshotko E (1991) Experimental study of boundary layer transition with elevated freestream turbulence on a heated flat plate. PhD thesis, Case Western Reserve University, also NASA CR 187086